ELSEVIER

Chemical Engineering Journal 141 (2008) 332–345

Chemical Engineering Journal

www.elsevier.com/locate/cej

Hollow self-inducing impellers for gas–liquid–solid dispersion: Experimental and computational study

B.N. Murthy, R.B. Kasundra, J.B. Joshi *

Department of Chemical Engineering, Institute of Chemical Technology, University of Mumbai, Matunga, Mumbai 400019, India

Received 18 August 2007; received in revised form 8 January 2008; accepted 23 January 2008

Abstract

In this work, experimental and computational fluid dynamic studies have been carried out for hollow self-inducing three-phase stirred tank systems. The effect of different impeller designs (hollow self-inducing pitched blade down flow turbines of different blade angles (PBTD30, PBTD45, PBTD60), and self-inducing modified double disc (MDD) impeller) and operating conditions such as solid loading (0–7 wt. %) and solid particle size (125–700 μm) have been investigated on critical impeller speed for solid suspension (N_{CS}), gas induction rate (Q_G) and overall gas hold-up ($\in_G$). Computational fluid dynamics model based on the Eulerian multi-fluid approach has been employed along with the standard k-ε turbulence model. A multiple reference frame (MRF) approach was used to model the impeller rotation. In this study, the multiphase flow has been simulated using a commercial CFD code, Fluent v6.2.16. A good agreement was found between the CFD predictions and the experimental values of N_{CS}.

Keywords: Stirred tank; CFD; Eulerian–Eulerian; Three-phase flows; Hollow self-inducing impeller

1. Introduction

Gas inducing impeller involving three phases, is a special design of a gas–liquid–solid contactor where utilization of the gas phase is complete. In this equipment, the impeller does three jobs simultaneously: gas induction, gas dispersion and also solid suspension. It eliminates the use of either external compressor (sparged loop reactor) or external pump (jet loop reactor) thus imparting the advantages of the safety, reliability and economy. Typical applications of gas inducing contactor include: catalytic hydrogenations, ammonolysis, oxidation, suspension polymerization, oxidative leaching of ores, waste water treatment, etc. There are many types of gas-inducing impellers reported in the literature, such as stator–rotor type and hollow impeller type. Comprehensive review of this subject has been provided by Patwardhan and Joshi [1]. The present work is concerned with the hollow impellers which have received less attention [2–4].

In some of these applications, the reaction occurs between a dissolved gas and a liquid phase reactant in the presence of a solid catalyst. In some other cases, the liquid is an inert medium and the reaction takes place between the dissolved gas and the solids. Such three-phase sparged stirred reactors have received wide attention during the past forty years and Kasat and Pandit [5] have extensively reviewed this subject. However, three-phase systems where the impeller does the job of gas induction, gas dispersion and also solid suspension, have been scarcely studied in the literature. On the other hand, the computational fluid dynamics (CFD) approach has attracted intensive attention in recent years for its capacity for understanding the flow patterns and the interactions between the gas–liquid and the solid–liquid phases. However, most of the literature on CFD simulations of flow field in stirred tanks is limited to single-phase and two-phase flows. In the case of three-phase systems, the interactions between the two dispersed phases and the contribution of dispersed phases on the turbulence of the continuous phase make the numerical solution of the governing equations more challenging.

The complexity of the flow generated in the system (3D, recirculating and often turbulent) has compelled the researchers, designers and the practicing engineers to resort to empirical approach for the design, scale-up and optimization of the mulitphase reactors. In order to reduce existing state of empiricism, during the past thirty years, an attempt is being made to under-

---

* Corresponding author. Tel.: +91 22 2414 5616; fax: +91 22 2414 5614.
E-mail address: jbj@udct.org (J.B. Joshi).

1385-8947/$ – see front matter © 2008 Elsevier B.V. All rights reserved.
doi:10.1016/j.cej.2008.01.040

Nomenclature

Notations

A	empirical constant
A_0	cross sectional area of orifice (m^2)
B	empirical constant
C	empirical constant
C_μ, $C_{\in 1}$, $C_{\in 2}$, $C_{\in 3}$	turbulence model constants
C_D	drag coefficient in turbulent liquid
C_{DO}	drag coefficient in still liquid
C_G	constant
C_L	constant
D	impeller diameter (m)
d_p	particle diameter (m)
d_B	bubble diameter (m)
g	acceleration due to gravity (9.8 m s^{-2})
H	liquid height (m)
k	turbulent kinetic energy (m^2 s^{-2})
F_D	drag force per unit area (N m^{-3})
N	impeller rotation speed (s^{-1})
N_{CS}	critical impeller speed for just suspension (rps)
N_{SG}	critical impeller speed for solid suspension in gas–liquid–solid system (rps)
P_K	turbulence production (kg m^{-1} s^{-3})
$\langle P\rangle$	pressure (pa)
Q_G	rate of gas induction (m^3 s^{-1})
T	tank diameter (m)
$\langle u\rangle$	average velocity (m s^{-1})
w	height of the impeller blade (m)
z	axial co-ordintae direction (m)

Greek letters

$\in$	volume fraction
ε	turbulent energy dissipated per unit mass (m^2 s^{-3})
λ	Kolomogoroff eddy size (m)
ρ	density of fluid (kg m^{-3})
μ	viscosity (kg m^{-1} s^{-1})
μ_{eff}	effective viscosity (kg m^{-1} s^{-1})
μ	gas particle induced viscosity of the liquid phase (kg m^{-1} s^{-1})
$\mu_{S,L}$	solid particle induced viscosity of the liquid phase (kg m^{-1} s^{-1})
μ	turbulent induced viscosity (kg m^{-1} s^{-1})
σ_k	turbulent Prandtl number for the turbulent kinetic energy
σ_ε	turbulent Prandtll number for the dissipation rate

Subscripts

G	gas phase
L	liquid phase
S	solid phase
r	radial co-ordinate direction
t	turbulent
tip	at the tip of the impeller blade

stand the underlying fluid mechanics and its relationship with the design parameters. In particular, the computational fluid dynamics (CFD) and the experimental fluid dynamics (EFD) have led to better understanding of the detailed hydrodynamics in single-phase flow systems. However, because of even additional complexities associated with the three-phase systems, scanty information is available on the CFD simulations as well as experimental efforts on flow visualization. Therefore, it was thought desirable to undertake a systematic investigation on the CFD simulations and some hydrodynamic measurements.

The objective of the present study is to provide experimental data on critical impeller speed for solid suspension, the rate of gas induction, and the overall gas hold-up for hollow self-inducing stirred reactor under different operating conditions and geometrical conditions. The objective is also to perform CFD simulations based on the Eulerian–Eulerian multi-fluid approach to predict the critical impeller speed for solid suspension, corresponding gas induction rate and the overall gas hold-up. Finally, the experimental data have been compared with the CFD predictions.

2. Experimental setup

The experimental setup is shown in Fig. 1. The tank geometry employed in this work is a flat bottomed cylindrical tank ($T = H = 0.50$ m) with four equally spaced baffles ($b = T/10$) and it is the same as that used by Deshmukh et al. [3]. Two impeller designs were employed: a hollow self-inducing pitched blade turbine (see Fig. 2A ($D = T/2$)) and a six bladed self-inducing modified double disc impeller (see Fig. 2B) with $D = T/3$. The impeller was located at a distance of $T/3$ from the tank base. The

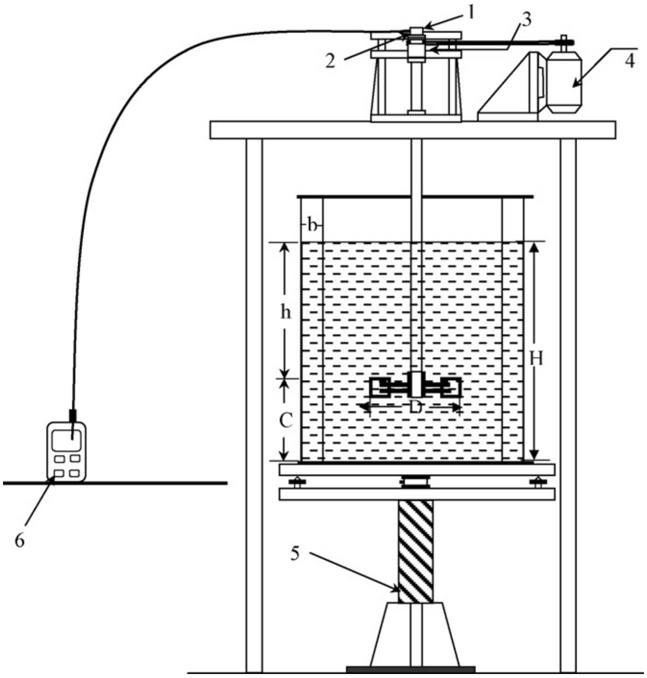

Fig. 1. Schematic diagram of experimental setup. (1) Inlet for gas induction; (2) anemometer turbine; (3) stuffing box; (4) thyristor controlled DC motor; (5) screw jack; (6) anemometer indicator.

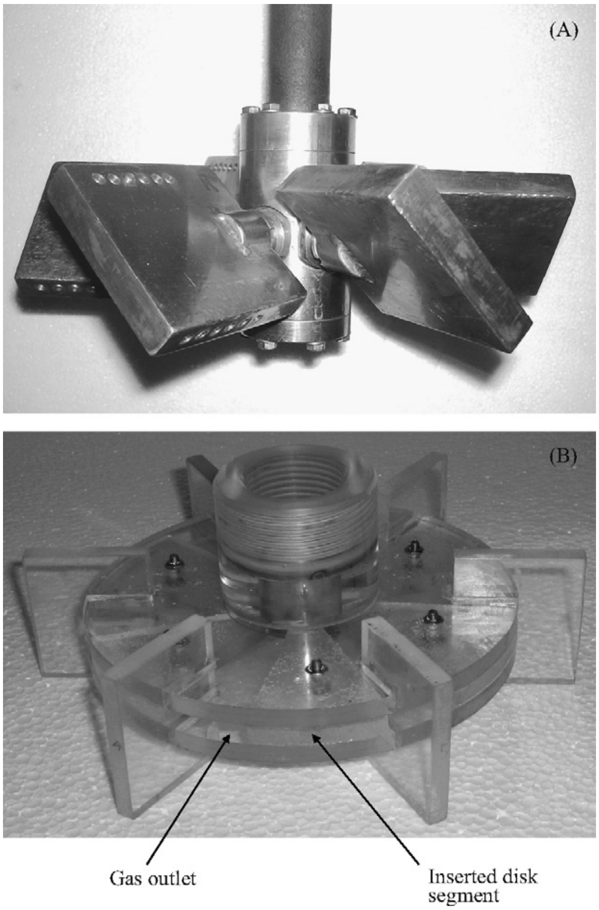

Fig. 2. Hollow impellers used for study. (A) Hollow PBTD impeller, (B) modified double disk impeller.

shaft and the impeller were hollow. The internal diameter of the shaft was 30 mm. Impeller rotation speed was measured with electronic meter having magnetic proximity probe for detecting shaft rotation. The speed could be read with an accuracy of 1 rpm. Critical impeller speed for gas induction was measured by visually observing the smallest speed when air bubbles were induced near the impeller. In the case of hollow self-inducing PBTD, the surface aeration also occurs with gas induction. For accurate measurement of critical impeller speed, a horizontal baffle was introduced near the gas–liquid interface and the surface aeration was arrested. The rate of gas induction was measured using pre-calibrated turbine type anemometer. The gas flow rate could be measured with an accuracy of 2%. Due to the intrinsic fluctuations with the gas induction process, each flow reading was taken ten times and reported as an average value. Glass beads of 125, 350 and 700 μm sizes were used as the solid phase. Solid loading was varied from 0 to 7 wt.%. The critical impeller speed required for solid suspension in gas–liquid–solid (N_{CS}) systems was defined as the speed at which none of the particles rest on the base of stirred tank for longer than 2 s [6,7]. The measurements of N_{CS} were made by visually observing the solid particles on the bottom by placing a mirror below the tank base which was illuminated.

3. CFD modeling

In the present work, 3D CFD simulations have been performed for the multiphase stirred tank. An Eulerian multi-fluid model has been adopted to describe the flow behaviour of each phase. In this model, gas, liquid and solid phases are all treated as different continua, interpenetrating and interacting with each other everywhere in the computational domain. Liquid is considered to be the continuous phase while gas bubbles and solid particles are considered to be the dispersed phases. In Fluent, the derivation of the conservation equations for mass and momentum for each of the three phases is done by phase weighted Favre-averaging [8] the local instantaneous values, and no additional turbulent dispersion term is introduced into the continuity equation. The pressure field is assumed to be shared by the three phases, in proportion to their volume fraction. The motion of each phase is governed by respective mass and momentum conservation equations.

The continuity equation for each phase is given by:

$$\frac{\partial(\rho_{\mathrm{G}} \in_{\mathrm{G}})}{\partial t} + \nabla \cdot (\rho_{\mathrm{G}} \in_{\mathrm{G}} \langle u_{\mathrm{G}} \rangle) = 0 \tag{1}$$

$$\frac{\partial(\rho_{\mathrm{L}} \in_{\mathrm{L}})}{\partial t} + \nabla \cdot (\rho_{\mathrm{L}} \in_{\mathrm{L}} \langle u_{\mathrm{L}} \rangle) = 0 \tag{2}$$

$$\frac{\partial(\rho_{\mathrm{S}} \in_{\mathrm{S}})}{\partial t} + \nabla \cdot (\rho_{\mathrm{S}} \in_{\mathrm{S}} \langle u_{\mathrm{S}} \rangle) = 0 \tag{3}$$

where ρ is the density, $\in$ is the volume fraction, and u is the velocity vector of each phase.

The momentum balance equation for each phase is:

$$\begin{aligned} &\frac{\partial(\rho_{\mathrm{G}} \in_{\mathrm{G}} \langle u_{\mathrm{G}} \rangle)}{\partial t} + \nabla \cdot (\rho_{\mathrm{G}} \in_{\mathrm{G}} \langle u_{\mathrm{G}} \rangle \langle u_{\mathrm{G}} \rangle) \\ &\quad = - \in_{\mathrm{G}} \nabla \langle p \rangle + \nabla \cdot \left(\in_{\mathrm{G}} \mu_{\mathrm{eff,G}} \left(\nabla \langle u_{\mathrm{G}} \rangle + (\nabla \langle u_{\mathrm{G}} \rangle)^{T} \right) \right) \\ &\qquad + \rho_{G} \in_{G} \vec{g} - F_{\mathrm{I,LG}} \end{aligned} \tag{4}$$

$$\begin{aligned} &\frac{\partial(\rho_{\mathrm{L}} \in_{\mathrm{L}} \langle u_{\mathrm{L}} \rangle)}{\partial t} + \nabla \cdot (\rho_{\mathrm{L}} \in_{\mathrm{L}} \langle u_{\mathrm{L}} \rangle \langle u_{\mathrm{L}} \rangle) \\ &\quad = - \in_{\mathrm{L}} \nabla \langle p \rangle + \nabla \cdot \left(\in_{\mathrm{L}} \mu_{\mathrm{eff,L}} \left(\nabla \langle u_{\mathrm{L}} \rangle + (\nabla \langle u_{\mathrm{L}} \rangle)^{T} \right) \right) \\ &\qquad + \rho_{\mathrm{L}} \in_{\mathrm{L}} \vec{g} + \vec{F}_{I,LG} + \vec{F}_{I,LS} \end{aligned} \tag{5}$$

$$\begin{aligned} &\frac{\partial(\rho_{\mathrm{S}} \in_{\mathrm{S}} \langle u_{\mathrm{S}} \rangle)}{\partial t} + \nabla \cdot (\rho_{\mathrm{S}} \in_{\mathrm{S}} \langle u_{\mathrm{S}} \rangle) \\ &\quad = - \in_{\mathrm{S}} \nabla \langle p \rangle + \nabla \cdot \left(\in_{\mathrm{S}} \mu_{\mathrm{eff,S}} \left(\nabla \langle u_{\mathrm{S}} \rangle + (\nabla \langle u_{\mathrm{S}} \rangle)^{T} \right) \right) \\ &\qquad + \rho_{\mathrm{S}} \in_{\mathrm{S}} \vec{g} - \vec{F}_{I,\mathrm{LS}} \end{aligned} \tag{6}$$

where p is the pressure μ_{eff} is the effective viscosity, g is the gravitational acceleration, and F_{I} is the interphase momentum transfer force. The phasic volume fractions satisfy the following condition:

$$\in_{\mathrm{G}} + \in_{\mathrm{L}} + \in_{\mathrm{S}} = 1 \tag{7}$$

3.1. Interphase momentum transfer

Interactions between the phases involve various momentum exchange mechanisms such as the drag, the lift and the added mass force, etc. However, the contribution of drag force has been considered while the effect of the other forces has been ignored [9–11].

The drag force exerted by the dispersed phase on the continuous phase is calculated as:

$$\vec{F}_{\mathrm{D,LG}} = \frac{3}{4}\frac{C_{\mathrm{D,LG}}}{d_{\mathrm{B}}} F\rho_{\mathrm{L}} \in_{\mathrm{G}} |\langle u_{\mathrm{G}}\rangle - \langle u_{\mathrm{L}}\rangle| (\langle u_{\mathrm{G}}\rangle - \langle u_{\mathrm{L}}\rangle) \tag{8}$$

$$\vec{F}_{\mathrm{D,LS}} = \frac{3}{4}\frac{C_{\mathrm{D,LS}}}{d_{\mathrm{p}}} \rho_{\mathrm{L}} \in_{\mathrm{S}} |\langle u_{\mathrm{S}}\rangle - \langle u_{\mathrm{L}}\rangle| (\langle u_{\mathrm{S}}\rangle - \langle u_{\mathrm{L}}\rangle) \tag{9}$$

Where C_{D} is the drag coefficient and d is the diameter.

The drag coefficient exerted by the gas phase on the liquid phase is obtained by the modified Brucato drag model [11], which is as follows:

$$\frac{C_{\mathrm{D}} - C_{\mathrm{DO}}}{C_{\mathrm{DO}}} = 8.76 \times 10^{-5}\left(\frac{d_{\mathrm{p}}}{\lambda}\right)^3 \tag{10}$$

The drag coefficient exerted by the solid phase on the liquid phase is calculated using the drag law proposed by Pinelli et al. [12], which is as follows.

$$\frac{C_{\mathrm{DO}}}{C_{\mathrm{D}}} = \left[0.4 \tan h\left(\frac{16\lambda}{d_{\mathrm{p}}} - 1\right) + 0.6\right]^2 \tag{11}$$

The drag coefficient in still liquid for the gas–liquid dispersion has been predicted using the following the expression.

$$C_{\mathrm{D0}} = \max\left\{\left(\frac{2.667 Eo}{Eo + 4.0}\right)\left(\frac{24}{Re_{\mathrm{b}}}(1 + 0.15 Re_{\mathrm{b}}^{0.687})\right)\right\} \tag{12}$$

Whereas, for the solid–liquid dispersion the following expression has been used.

$$C_{\mathrm{D0}} = \left(\frac{24}{Re_{\mathrm{p}}}(1 + 0.15\,\mathrm{Re}_{\mathrm{p}}^{0.687})\right) \tag{13}$$

3.2. Turbulence closure

In the present work, the standard model for single-phase flows has been extended for the three-phase flows with extra terms that include interphase turbulent momentum transfer to take into account the effects of turbulence. Further, it has been assumed that the turbulence in multiphase stirred tanks is mainly presented in the continuous phase. It is known from the literature that both the gas–liquid and liquid–solid two-phase flows have been successfully simulated by the standard k-ε turbulence model with mixture properties to calculate the turbulent viscosity of the mixture. The governing equations for the turbulent kinetic energy (k) and the energy dissipation rate (ε) are given by:

$$\frac{\partial \in_{\mathrm{L}}\rho_{\mathrm{L}}k_{\mathrm{L}}}{\partial t} + \frac{\langle u_{\mathrm{i}}\rangle\, \partial(\in_{\mathrm{L}}\rho_{\mathrm{L}}k_{\mathrm{L}})}{\partial x_{\mathrm{i}}} = \nabla\left(\in_{\mathrm{L}}\left(\mu + \frac{\mu_{\mathrm{t,L}}}{\sigma_{\mathrm{kL}}}\right)\nabla k_{\mathrm{L}}\right) + \in_{\mathrm{L}}\rho_{\mathrm{L}}(P_{\mathrm{kL}} - \varepsilon_{\mathrm{L}}) + \Pi_{\mathrm{kL}} \tag{14}$$

$$\frac{\partial \in_{\mathrm{L}}\rho_{\mathrm{L}}\varepsilon_{\mathrm{L}}}{\partial t} + \frac{\langle u_{\mathrm{i}}\rangle\, \partial\langle \in_{\mathrm{L}}\rho_{\mathrm{L}}\varepsilon_{\mathrm{L}}\rangle}{\partial x_{\mathrm{i}}} = \nabla\left(\in_{\mathrm{L}}\left(\mu + \frac{\mu_{\mathrm{t,L}}}{\sigma_{\varepsilon\mathrm{L}}}\right)\nabla \varepsilon_{\mathrm{L}}\right) + \in_{\mathrm{L}}\rho_{\mathrm{L}}\frac{\varepsilon_{\mathrm{L}}}{k_{\mathrm{L}}}(C_{\varepsilon 1}P_{\mathrm{kL}} - C_{\varepsilon 2}\varepsilon_{\mathrm{L}}) + \Pi_{\varepsilon\mathrm{L}} \tag{15}$$

Diffusion of momentum in each phase is governed by an effective viscosity:

$$\mu_{\mathrm{eff,L}} = \mu_{\mathrm{L}} + \mu_{\mathrm{t,L}} + \mu_{\mathrm{G,L}} + \mu_{\mathrm{S,L}} \tag{16}$$

$$\mu_{\mathrm{eff,G}} = \mu_{\mathrm{G}} + \mu_{\mathrm{t,G}} \tag{17}$$

$$\mu_{\mathrm{eff,S}} = \mu_{\mathrm{S}} + \mu_{\mathrm{t,S}} \tag{18}$$

Where μ is the molecular viscosity, μ_{t} is the turbulent viscosity and $\mu_{\mathrm{G,L}}$, $\mu_{\mathrm{S,L}}$ are the particle (gas bubble and solid particle) induced viscosities of the liquid phase. The turbulent viscosity of the continuous phase is obtained by the k-ε model:

$$\mu_{\mathrm{t,L}} = C_{\mu}\rho_{\mathrm{L}}\left(\frac{k^2}{\varepsilon}\right) \tag{19}$$

The additional particle induced eddy viscosities to the continuous phase are:

$$\mu_{\mathrm{G,L}} = C_{\mu\mathrm{p}}\rho_{\mathrm{L}} \in_{\mathrm{G}} d_{\mathrm{G}}\, |\langle u_{\mathrm{G}}\rangle - \langle u_{\mathrm{L}}\rangle| \tag{20}$$

$$\mu_{\mathrm{S,L}} = C_{\mu\mathrm{p}}\rho_{\mathrm{L}} \in_{\mathrm{S}} d_{\mathrm{S}}\, |\langle u_{\mathrm{S}}\rangle - \langle u_{\mathrm{L}}\rangle| \tag{21}$$

The turbulent viscosity of the dispersed phase is calculated using the zero equation model:

$$\mu_{\mathrm{t,G}} = \frac{\rho_{\mathrm{G}}}{\rho_{\mathrm{L}}}\mu_{\mathrm{t,L}} \tag{22}$$

$$\mu_{\mathrm{t,S}} = \frac{\rho_{\mathrm{S}}}{\rho_{\mathrm{L}}}\mu_{\mathrm{t,L}} \tag{23}$$

The values of the constants are the standard ones: $C_{\varepsilon 1} = 1.44$, $C_{\varepsilon 2} = 1.92$, $C_{\mu} = 0.09$, $C_{\mu\mathrm{p}} = 0.6$, $\sigma_{\mathrm{k}} = 1.0$, $\sigma_{\varepsilon} = 1.3$. The value of the molecular viscosity of solid phase is set to be the same as that of the water, since its variations do not bring obvious changes to the simulation results.

4. Method of solution

4.1. Flow field

Steady state simulations were carried out for different types of impellers, wide range of agitation speeds, solid particle sizes, and solid loading and induction rates. The details of the reactor geometry and the operating parameters have been summarized in Table 1. In this work, all the simulations have been performed using the commercially available CFD software Fluent v6.2.16. The set of governing equations are solved by a finite control volume technique. In the present study, entire geometry has been considered for the simulations. The multiple reference frame method has been used for the impeller modeling. For all the simulations, the boundary of the rotating domain was positioned at $r = 0.16$ and $0.10\,\mathrm{m} \le z \ge 0.24\,\mathrm{m}$. Tetrahedral elements were

Table 1
Geometrical details

Impeller type	Impeller diameter (D (m))	Tank diameter (T (m))	Liquid height (H (m))	Clearance from bottom (C (m))
Hollow PBTD30	0.25	0.5	0.5	0.17
Hollow PBTD45	0.25	0.5	0.5	0.17
Hollow PBTD60	0.25	0.5	0.5	0.17
Double disk impeller	0.17	0.5	0.5	0.17

used for meshing the geometry and a good quality of mesh was ensured throughout the computational domain using the GAMBIT mesh generation tool. As regards to the mesh quality, we have been restricted to use the tetra mesh element due to the large number of case studies under consideration and also because of complex geometry. However, in this study, a very high quality of mesh (skewness < 0.7) has been ensured throughout the computational domain. The number of grid elements in all the three directions in the impeller as well as the outer zone were systematically increased. When refining the mesh, care was taken to put most additional mesh element in the regions of high gradient around the blades and the discharge region. In order to check the sensitivity of the simulation result on the grid size, the grid spacing was reduced by a factor of two. Comparison of the two cases showed that the reduction of the grid size did not generate a noticeable difference in the simulation results. Therefore, grid elements in the range of 600,000–700,800 have been used in all the studies. Regarding boundary conditions, tank walls, the impeller surfaces and the baffle surfaces have been treated as no-slip boundary condition and the standard wall functions have been employed.

In a gas–liquid stirred vessel, there may be a wide distribution of bubble sizes. The prevailing bubble size distribution in a gas–liquid stirred vessel is controlled by several parameters like vessel, impeller design, impeller speed and induction rate. It is possible to develop a detailed multi-fluid computational model using the population balance framework to account for the bubble size distribution. We have developed, applied and validated such models for gas–liquid flow in bubble columns [13]. However, use of multi-fluid models based on population balances increase the computational demands by many fold. Unfortunately available experimental data of bubble size distribution in stirred vessel is not adequate to calculate the parameters appearing in coalescence and break-up kernels. Apart from the uncertainty in parameters of coalescence and break-up kernels, there is significant uncertainty in estimation of interphase drag force on gas bubbles in presence of other bubbles and high levels of turbulence prevailing in the vessel. Considering these issues and the present state of understanding, the option of using a multi-fluid model for stirred vessels is premature especially since the experimental data on bubble size distribution is available in the published literature. However, we have performed CFD simulations for different fixed bubble sizes, a bubble size of 3 mm was found to give reasonable agreement with the experimental data of the present work.

At a liquid surface, a small gas zone was added at the free surface of water, a method that has been reported to dampen instabilities [14] and only gas is allowed to escape using pressure outlet boundary condition which means top surface being exposed to atmospheric pressure. It was initially assumed that the particles were uniformly distributed in the liquid. All terms of the governing equations are discretised using the QUICK scheme. The SIMPLE algorithm has been employed for the pressure-velocity coupling. The convergence criterion (sum of normalized residuals) was set at 10^{-4} for all the equations. All the simulations have been simultaneously carried out on the 16 node, 32 processors AMD64 cluster with a clock speed of 2.4 GH and 2 GB memory with each node. Total Simulation time for each case was around 120 h.

4.2. Rate of gas induction

Determination of gas induction rate (Q_G) is an important step in designing the three-phase hollow impeller system. When the impeller speed is zero, the level of liquid in hollow pipe and in the vessel is the same (in Deshmukh et al. [3], Fig. 1). As the impeller speed increases, at any point on the impeller, pressure reduction occurs due to an increase in the kinetic head according to Bernoulli's equation. At critical impeller speed (N_{CG}), the reduction in pressure at the outlet of orifice on each impeller blade is sufficient to overcome the static head of liquid and the gas is just induced. The gas induction rate depends on the pressure driving force (local pressure at the orifice-head space pressure) generated due to impeller rotation. From the above discussion it is clear that the local pressure at the orifice is an important parameter that determines the rate of gas induction. Once the gas starts to induce into the solid–liquid mixture the local pressure field itself is altered. This occurs mainly due to the gas–liquid–solid interactions in the impeller zone.

The present work adopted an iterative method for calculating the gas induction rate (Murthy et al. [4]). This method involves carrying out the CFD simulations for the two independent geometries, i.e., single-phase simulations for hollow shaft and impeller together and three-phase simulations for the stirred tank.

5. Results and discussions

5.1. Two-phase flows

It was thought desirable to confirm the validity of the model for the two extreme cases of gas–liquid and solid–liquid dispersions. For a gas–liquid system, particle image velocimetry (PIV) data of Aubin et al. [15] have been used for the comparison of radial profiles of the mean axial velocity at various axial locations generated by PBTD45 with $D/T = 0.5$. The above

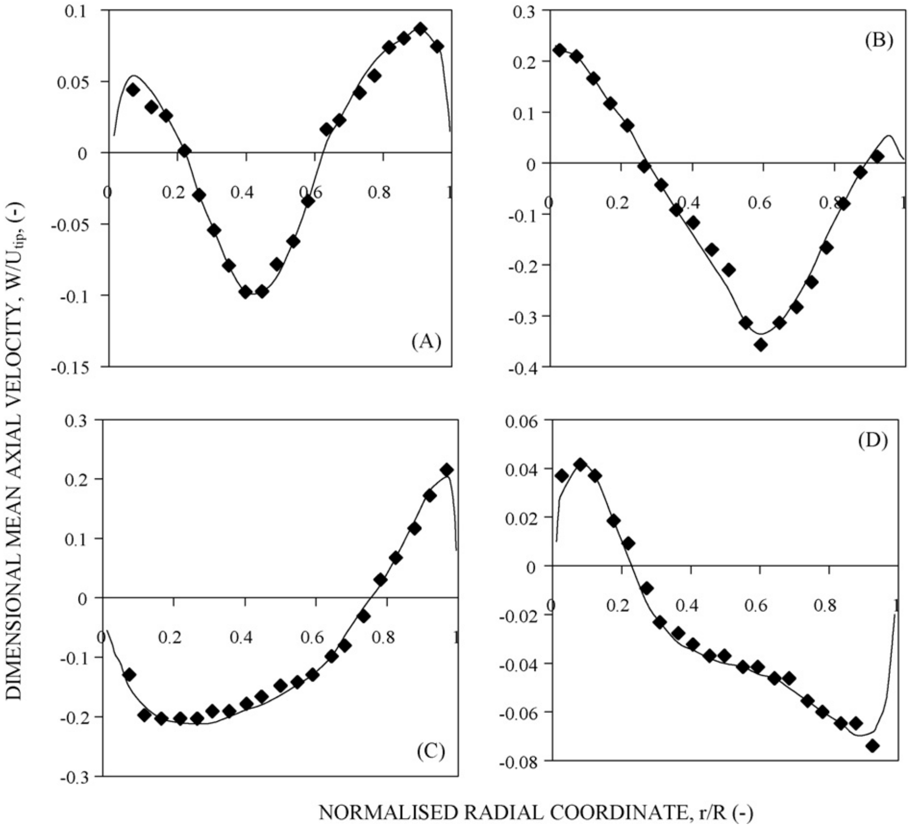

Fig. 3. Comparison between the simulated and experimental profiles of the dimensionless mean axial velocity for PBTD45 at various axial levels. (A) $z/T = 0.19$ m; (B) $z/T = 0.31$ m; (C) $z/T = 0.49$ m; (D) $z/T = 0.65$ m: (♦) experimental; (—) CFD predictions.

simulations have been carried out using the modified Brucato drag model [11] with an appropriate grid resolution. Fig. 3 ($z/T = 0.19$ (A), 0.31 (B), 0.49 (C) and 0.65 (D)) show an excellent agreement between the predictions and experimental data. For solid–liquid systems, Pinelli et al. [12] drag model was used. From Fig. 4A it can be seen that the CFD predictions of the axial solid concentration profiles are in good agreement with the experimental measurements of Barresi and Baldi [16]. The influence of solid particle concentration on the mean liquid velocity has been studied using CFD and compared with the experimental data of Angst et al. [17]. It can be seen in Figs. 4B–D that the present model has predicted the decrease in the mean liquid velocity (at $z/T = 0.40$) with an increase in the solid concentration (1, 2 and 3 vol%) which is in good agreement with the experimentally measured velocities.

5.2. *Gross flow field*

The gas–liquid–solid flows generated by self-inducing MDD, PBTD60, PBTD45 and PBTD30 impellers have been computed for a solid loading of 3 wt.% ($d_p = 125\ \mu$m) and for the impeller speeds (N) above the respective critical speeds for solid suspension (7, 8, 5 and 4 rps). The predicted liquid–velocity vectors have been depicted in Fig. 5A–D, for all the four impellers. It can be observed that the present CFD model is able to capture all the qualitative flow features generated by various impellers. Fig. 5A shows that, in the case of MDD impeller, similar to Rushton turbine, the liquid flow leaving the impeller travels in the radial direction and near the wall, splits into two streams. Each stream creates a circulation loop, one below and one above the impeller. Only a part of the energy supplied by the impeller, which is associated with lower loop, is available in the bottom region for performing various functions such as solid suspension. Self-inducing PBTD30 and PBTD45 impellers (Fig. 5B) generate one circulation loop where the flow leaving the impeller is downward towards the bottom of the tank, and is directly available for the suspension. However, in case of self-inducing PBTD60, the radial jet leaves with a certain angle with respect to impeller horizontal plane and near the vessel side wall (below the impeller (T/4 from bottom)) splits into two streams. Each stream creates a circulation loop, one below and one above the impeller. Only a part of the energy supplied by the impeller, which is associated with lower loop, is available in the bottom region for performing solid suspension. Therefore, the length of the liquid path and the number of direction changes are greater in the case of self-inducing PBTD60 and MDD as compared that for self-inducing PBTD45 and PBTD30 flow. As a result, the energy associated with the self-inducing PBTD45 and PBTD30 flow (in the bottom region) is much higher than the PBTD60 and MDD flow and hence the turbulence intensity for the self-inducing PBTD45 and PBTD30 impeller is also relatively high. Therefore, in the present case, self-inducing PBTD45 and PBTD30 impellers are relatively more efficient for solid suspension under

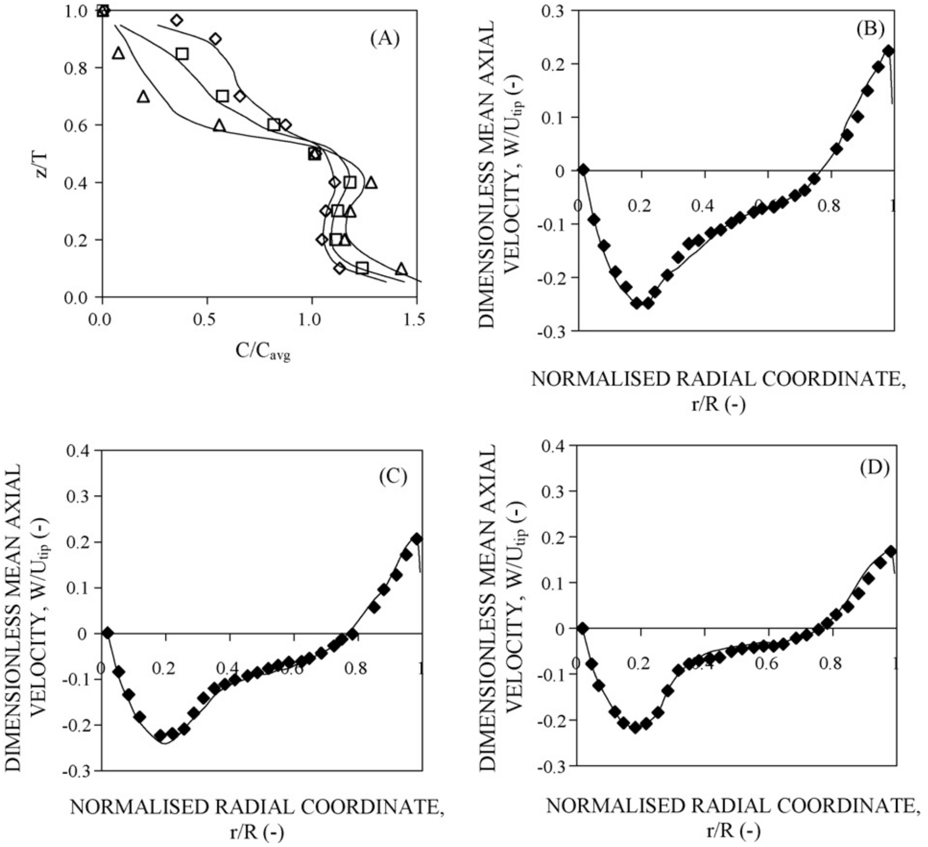

Fig. 4. (A) Comparison of experimental and predicted axial solid concentration profiles at N_{CS} of different particle sizes (◇: $d_p = 100$–$177\ \mu$m; □: $d_p = 208$–$250\ \mu$m; △: $d_p = 417$–$500\ \mu$m) for 4-PBTD. (B) Comparison of experimental and predicted dimensional mean axial profiles with mean dispersed phase volume fractions of (B) 1 vol%, (C) 2 vol%, and (D) 3 vol%, stirrer speed $1000\ s^{-1}$: (◆) experimental, (—) CFD predictions.

otherwise identical design and operating parameters (*T*, *D*, *C*, *H*, *P*/*V*, etc.).

The CFD predictions of the average gas hold-up ($\in_G$) have been compared with the experimentally measured data for self-inducing PBTD60 in Table 2. The present three-phase CFD model was found to under predict the $\in_G$ values. However, the qualitative CFD predictions were in good agreement with the experimental observations. Fig. 6A and B for self-inducing MDD impeller, and Fig. 6C and D for PBTD60 show the computed $\in_G$ in the impeller centre plane and in a vertical plane containing the impeller, respectively. It can be observed from the figures that the gas induced through the holes follows impeller discharge stream. The flow pattern shows the gas accumulation in the recirculating flow regions both above and below impeller centre plane. Further, in the low pressure region behind the impeller blades gas tends to accumulate and forming the so called gas cavities. It can be seen that satisfactory agreement is found between the simulated overall gas holdups and experimental observations.

Table 2
Experimental and predicted values of overall gas hold-up (PBTD60, $X = 1$ wt.%, $d_p = 125\ \mu$m, $\rho_p = 2400$)

Impeller speed N (s^{-1})	% Gas hold-up ($\in_G$)	
	Experimental	CFD
4	7	5
5	12.8	9.8
6	14	11
7	22	16

5.3. Solid suspension studies

Scanty information is available in the published literature on EFD and CFD studies of suspension of solid particles in a three-phase self-inducing gas–liquid–solid systems. Therefore, it was thought desirable to undertake systematic experimental measurements and CFD simulation of three-phase stirred dispersions. The simulations have been validated by comparing the CFD predictions and the experimental measurements of critical impeller speed for solid suspension over a wide range of design and operating conditions (Table 1). In the Eulerian–Eulerian approach, as used in this work, it is difficult to incorporate Zwietering's criterion in the CFD simulation of critical impeller speed for solid suspension. Therefore, we have extended the method proposed by Bohnet and Niesmak [18] for solid–liquid system, which has been based on the value of standard deviation of solid concentration. The same methodology has successfully been employed by Oshinowo and Bakker [19], Khopkar et al. [20], Bohnet and Niesmak [18], and they quantified the suspen-

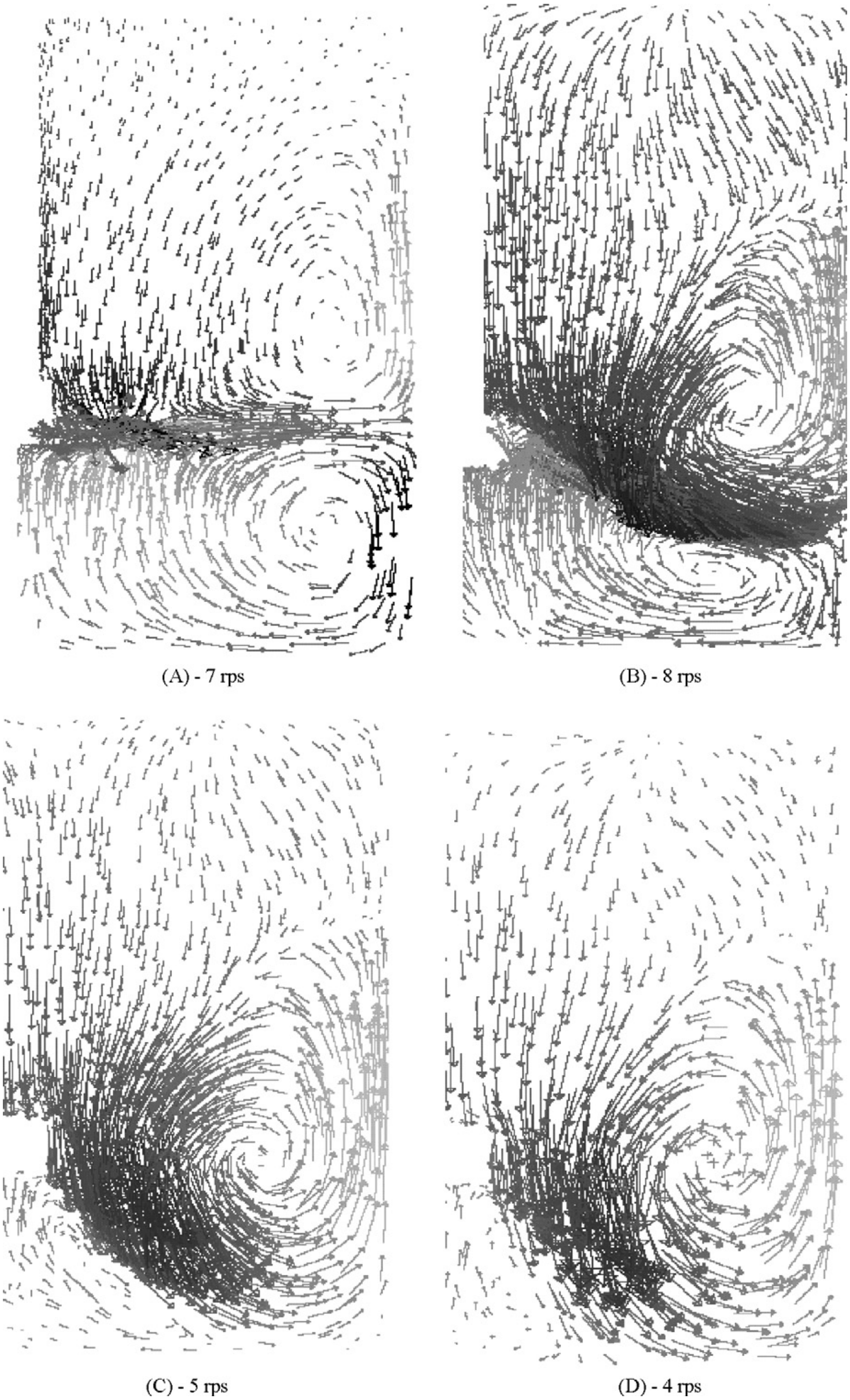

(A) - 7 rps

(B) - 8 rps

(C) - 5 rps

(D) - 4 rps

Fig. 5. Axial velocity vectors for liquid in presence of gas and solid in the mid plane between two baffles. (A) MDD; (B) PBTD60; (C) PBTD45; (D) PBTD30.

sion quality using the standard deviation defined as:

$$\sigma = \sqrt{\frac{1}{n}\sum_{1}^{n}\left(\frac{\in_{\mathrm{S}}}{\bar{\in}_{\mathrm{S}}} - 1\right)^{2}} \qquad (24)$$

Where n is the number of sampling locations used for measuring the solid phase hold-up. The increase in the degree of homogenization (better suspension quality) is manifested as the reduction of the value of standard deviation. On the basis of the quality of the suspension, the range of the standard deviation has been broadly divided into three ranges [17]. For uniform (homogeneous) suspensions, the value of the standard deviation is found to be smaller than 0.2 ($\sigma < 0.2$). However, for the "just suspension condition", the value of the standard deviation lies between 0.2 and 0.8 ($0.2 < \sigma < 0.8$), and for an incomplete suspension, $\sigma > 0.8$.

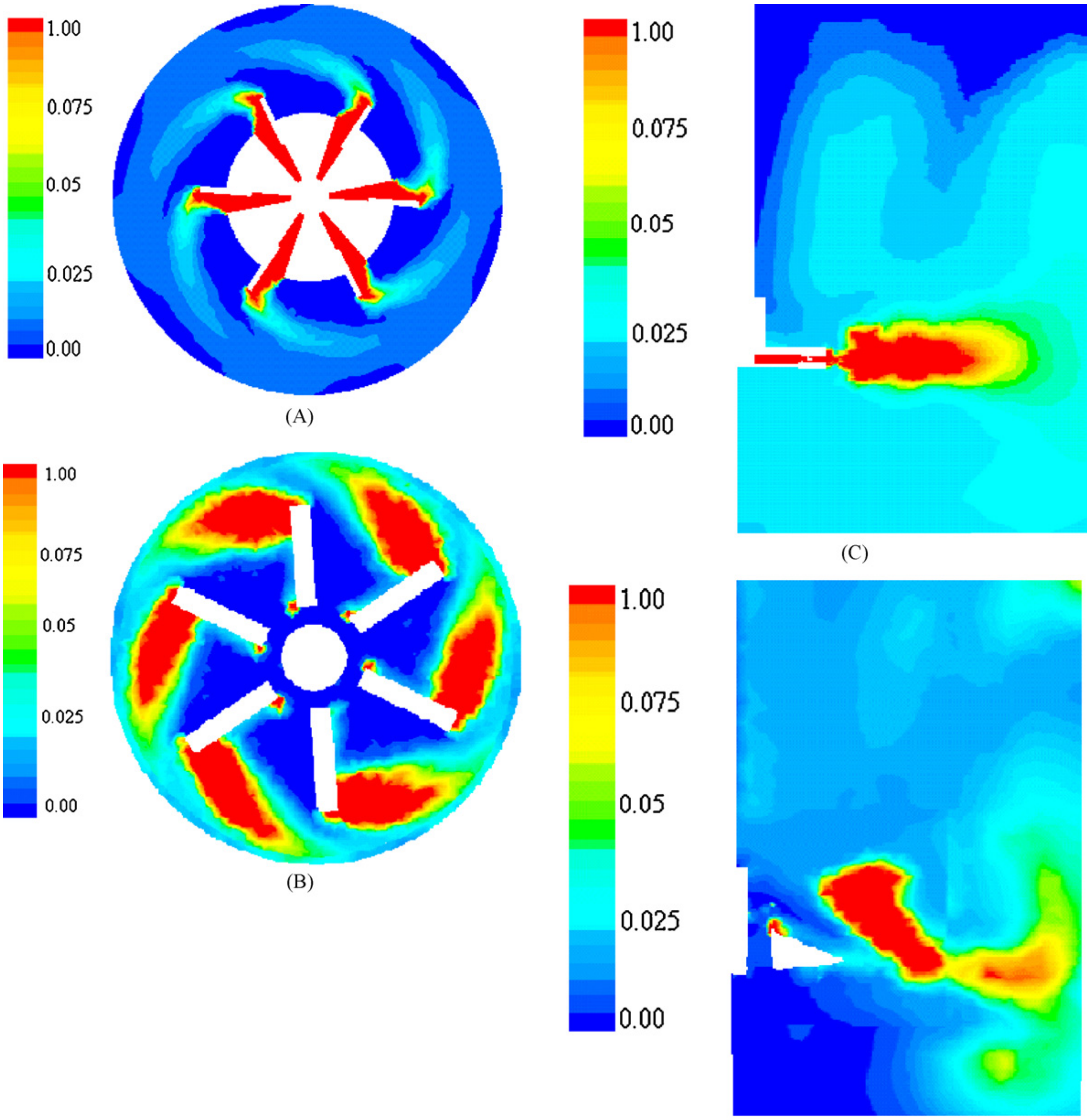

(A)

(B)

(C)

(D)

Fig. 6. CFD simulations of three-phase hollow self-inducing impeller system. (A) Contours of gas volume fraction (MDD: $N = 5.93$ rps, $X = 1$ wt.%, $d_p = 125$ μm) in the horizontal impeller center plane; (B) Contours of gas volume (PBTD60: $N = 6.4$ rps, $X = 1$ wt.%, $d_p = 125$ μm) fraction in the horizontal impeller center plane; (C) Contours of gas volume fraction (MDD: $N = 5.93$ rps, $X = 1$ wt.%, $d_p = 125$ μm) in the mid-plane between two baffles; (D) contours of gas volume fraction (PBTD60: $N = 6.4$ rps, $X = 1$ wt.%, $d_p = 125$ μm) in the mid-plane between two baffles.

CFD simulations were performed to calculate the values of the standard deviation using Eq. (24) for all the four impeller designs using 3 wt.% solid loading and 125 μm size particles. In the present study, the standard deviation was calculated using the values of $\in_s$ stored at all computational cells. Fig. 7 shows the variation of the standard deviation with respect to impeller speed. It can be noted that there is a reduction in the standard deviation as the impeller speed approaches N_{CS}. At N_{CS}, the variation of σ with respect to speed was found to reduce. In other words, the value of $d\sigma/dN$ was found to change at N_{CS}. Using this criterion, the values of N_{CS} for self-inducing MDD, PBTD60, PBTD45 and PBTD30 impellers ($X = 3\%$, $d_p = 125$ μm), were found to be 6.7 (0.73), 7.4 (0.70), 4.4 (0.68), and 3.8 (0.65) rps, respectively. The bracketed values are of standard deviation for that impeller at N_{CS}. For higher solid loading, i.e. 7 wt.% and the average particles size of 700 μm, it was computationally noted that the above set values of standard deviation for the N_{CS} believed to fall in the same range. It was due to increase in the solid loading from 3 to 7 wt.% and the average particles size from 125 to 700 μm, would not significantly alter the fluid mechanics in the vessel. Therefore, the abovementioned σ values have been used in rest of the paper for the estimation of N_{CS} using CFD simulations.

Further, with an increase in the impeller speed, the value of σ decreases rather slowly. This means, at a constant loading of solid particles when the impeller speed is gradually increased, beyond N_{CS}, more particles get suspended. It is well know that the position of solids on the tank bottom ($N > N_{CS}$) depends on the impeller design as different impellers generate different

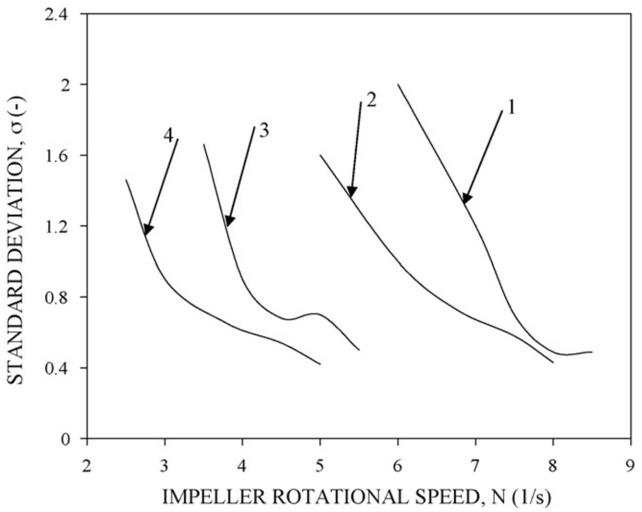

Fig. 7. CFD predicted values of the standard deviation with respect to impeller rotational speed. (1) MDD; (2) PBTD60; (3) PBTD45; (4) PBTD30 (3% solid loading, 125 μm).

flow patterns, and hence, offer different efficiencies for the suspension operation. In order to understand the quantitative role of the impeller design, both experiments and CFD simulations have been carried out for the different impeller designs (self-inducing MDD, PBTD60, PBTD45 and PBTD30) over a wide range of operating conditions.

It can be noted that the position of solids on the tank bottom ($N > N_{CS}$) depends on the impeller design. It can be clearly seen from Fig. 8 that, in the case of self-inducing MDD and PBTD60 impellers, the particles are suspended from an annular space around the center of the tank bottom, whereas for PBTD45 and PBTD30 self-inducing impellers suspension occurs from the periphery of tank bottom. It is evident that the impeller speed required for suspension by a PBTD30 self-inducing impeller (in fact P/V) is much lower than that required by PBTD60 and MDD self-inducing impellers. Further, for self-inducing MDD and PBTD60 impellers the present CFD model predicts a significant quantity of unsuspended particles present on the tank bottom. This shows that, at N_{CS}, PBTD30 self-inducing impeller is more efficient than the other three impellers.

5.3.1. *Effect of impeller design*

Earlier it has been shown that self-inducing MDD, PBTD60, PBTD45 and PBTD30 impellers generate different flow patterns, and hence, offer different efficiencies for the suspension operation. In order to understand the quantitative role of the impeller design, CFD simulations have been carried out for the four impeller designs and at different impeller speeds. For brevity, qualitative results are shown in the Fig. 8A–D at the critical impeller speeds. It has been noted that, with an increase in the impeller rotational speed, the amount of solid particles present at the bottom of the reactors has decreased. However, the increased impeller speed has marginal influence on the solids distribution in top 1/4th of the reactor. The values of the standard deviation have been calculated using Eq. (24). Fig. 9 shows the predictions of critical impeller speeds using CFD (when $\sigma = 0.69$) for all the impeller designs ($X = 5$ wt.%, the average particle size of 125, 350, and 700 μm), which have been in good agreement with the experimentally measured critical impeller speeds. It can be noted that PBTD60 and MDD self-inducing impellers require higher speeds than PBTD45 and PBTD30 self-inducing impellers. It is due to, in the case of PBTD60 and MDD self-inducing impellers (Fig. 5A and B), the liquid flow leaving the impeller travels in the radial direction and near the wall, splits into two streams. Each stream creates a circulation loop, one below and one above the impeller. Only a part of the energy supplied by the impeller, which is associated with lower loop, is available in the bottom region for performing various functions such as solid suspension. Where as PBTD45 and PBTD30 self-inducing impellers (Fig. 5C and D) generates one circulation loop where the flow leaving the impeller is downward towards the bottom of the tank, and is directly available for the suspension. The length of the liquid path and the number of direction changes are greater in the case of PBTD60 and MDD as compared that for PBTD45 and PBTD30 flow. As a result, the energy associated with the PBTD45 and PBTD30 flow (in the bottom region) is much higher than the PBTD60 and MDD flows and hence the turbulence intensity for the PBTD45 and PBTD30 self-inducing impellers is also relatively high. Therefore, PBTD45 and PBTD30 self-inducing impellers are relatively more efficient under otherwise identical design and operating parameters (T, D, C, H, P/V, V_G, etc.).

5.3.2. *Effect of particle size*

The critical impeller speed for solid suspension also depends upon the particle size. Therefore, it was thought desirable to study for various particle sizes. Experiments have been carried out for the three particle diameters, i.e., 125, 350 and 700 μm with PBTD45 self-inducing impeller, and for solid loading of 5 wt.%. For the same geometrical and operating conditions CFD simulations have been performed. Fig. 10 shows a good agreement between the CFD predictions and experimentally measured data for all the impeller designs. Further, it confirms the fact that, for a given tank and impeller configuration and for fixed set of operating conditions, uniformity of solids increases with a decrease in the particle size. With increasing particle size the settling velocity increases and there is a decrease in the homogeneity of the suspension. Therefore, higher average liquid velocity is required to suspend the particles.

5.3.3. *Effect of solid loading*

Experiments have been carried out to investigate the effect of solid loading on the critical impeller speed for solid suspension. For this, particles of average diameter 125 μm with solid loadings of 1, 3, 5 and 7 wt.%, respectively, have been considered (with PBTD45). CFD simulations have also been performed for the same geometrical and operating conditions. Fig. 11 shows a fairly good agreement between the CFD predicted and the experimentally measured values of N_{CS} ($d_p = 125$ μm). It can be noted that N_{CS} increases with increasing solid loading. This is because, some of the impeller energy dissipates at the solid–liquid interface.

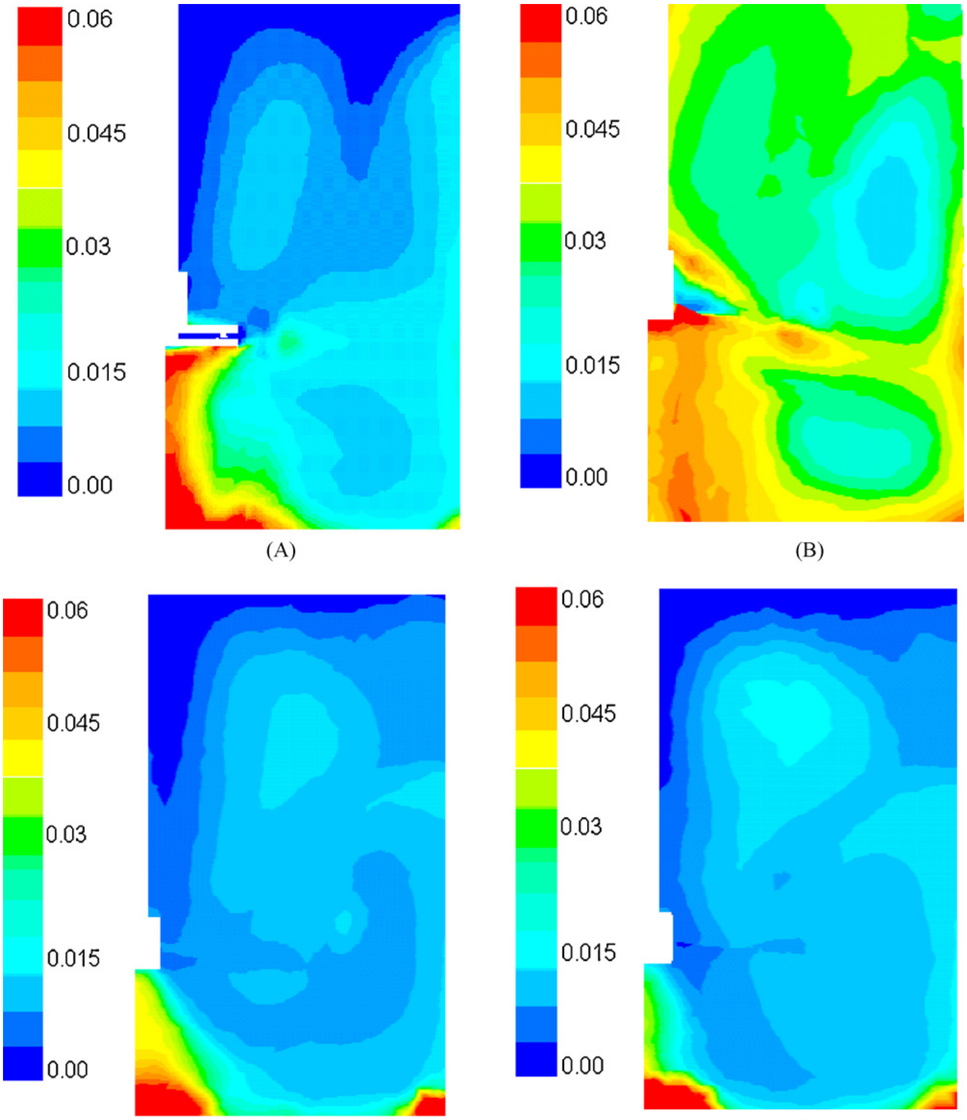

(A) (B)

(C) (D)

Fig. 8. Contours of solid volume fraction for (A) MDD; (B) PBTD60; (C) PBTD45 and (C) PBTD30 at N_{CS} by CFD simulations ($d_p = 350\,\mu m$, $\rho_p = 2400\,kg/m^3$, 5 wt.%).

5.4. Gas inducing rate

From the point of view design of gas inducing reactors, the dispersion of the induced gas is also an important aspect with suspending solids that governs the performance of three-phase hollow self-inducing contactors. In the foregoing section, detailed CFD simulations were reported for the prediction of N_{CS} which is the subject of this paper. Therefore, the rate of gas induction (Q_G) was measured at N_{CS} for all the four impellers for solid particles of 125, 350 and 700 μm sizes and solid loading was varied from 0 to 7 wt. %. Further, CFD simulations have also been performed to predict the gas induction rate and compared with experimentally measured data. It may again be pointed out that the values of Q_G (predicted as well as experimental) have been under the critical suspension condition. Therefore, any variable which affects N_{CS}, also affects Q_G. As a consequence, the following discussion brings out the effects of impeller diameter, d_p and X on Q_G, however, at N_{CS} in all the cases.

5.4.1. Effect of impeller design

One of the most important variables influencing the rate of gas induction is the impeller design. The gas induction rates measured at N_{CS} for different impeller designs under consideration are reported in Table 3 ($d_p = 125\,\mu m$, $X = 1$ wt %). The gas induction characteristic of any impeller depends on two main factors, pressure driving force created by impeller and dispersing ability

Table 3
Effect of impeller type on gas induction rate at N_{CS} for ($d_p = 125\,\mu m$, $\rho_p = 2400\,kg/m^3$, 1 wt.%)

Impeller type	N_{CS} (s^{-1})	Gas induction rate $Q_G \times 10^3$ (m^3/s)	
		Experimental	CFD
DDT	5.9	0.63	0.52
PBTD60	6.4	6.23	5.0
PBTD45	3.9	0.7	0.52
PBTD30	3.3	0.4	0.3

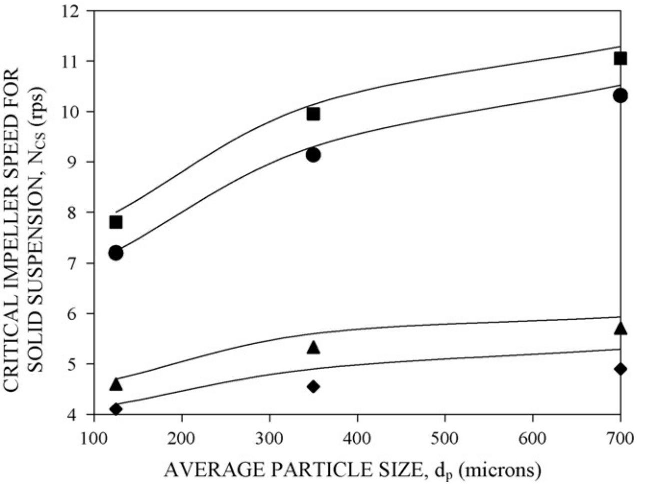

Fig. 9. Comparison of experimental and predicted critical impeller speeds for different impeller designs ($X = 5$ wt.%, the average particle size of 125, 350, and 700 μm). (◆) PBTD30; (▲) PBTD45; (■) PBTD60; (●) MDD; (—) CFD.

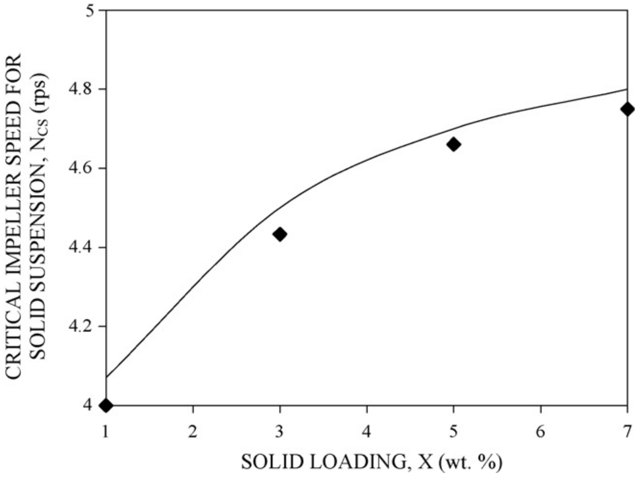

Fig. 11. Effect of solid loading on the critical impeller speed for PBTD45 ($d_p = 125$ μm, $\rho_p = 2400$ kg/m^3): (◆) experimental, (—) CFD predictions.

of the impeller. Impeller having higher power number tends to give more pressure driving force and at the same time consumes more power. Gas dispersing ability of impeller greatly affects the rate of gas induction as the local gas hold up decides the driving force for gas induction. Another factor which decides dispersing ability of impeller is its liquid pumping ability, as the flow created by the impeller drives the gas bubbles throughout the liquid volume. Experimentally it has been observed that the rate of gas induction for self-inducing PBTD30, PBTD45, PBTD60 and MDD impellers, increases uniformly with increasing impeller speed due to increase in the local driving force (decrease in the local pressure). Further, the present three-phase CFD model has been extended to predict the gas induction rate as it was explained in Section 4.2. Table 3 shows the predicted values of the Q_G and which have been slightly unpredicted as compared to experimental data for all the four impeller designs with $d_p = 125$ μm, $X = 1$ wt.%.

5.4.2. Effect of particle size

The gas induction measurements have been carried at N_{CS} for the three particle diameters, i.e., 125, 350 and 700 μm with MDD self-inducing impeller, and for solid loading of 5 wt.%. CFD simulations have been performed for the same and Fig. 12 shows the obvious increase in gas induction rate with increasing N_{CS} as the average particle size increases. The present CFD model was capable of predicting Q_G quantitatively despite the prevailing complex hydrodynamics. However, the discrepancy between the predicted and the experimentally measure Q_G was probably because the model of inter-phase momentum exchange employed in the present work is too simple to describe the real complex inter-phase interaction coupling in gas–liquid–solid three-phase flows. Additionally, the isotropic k-ε two equation turbulence model is deficient in describing the well-recognized anisotropic nature of turbulent flow in stirred tanks.

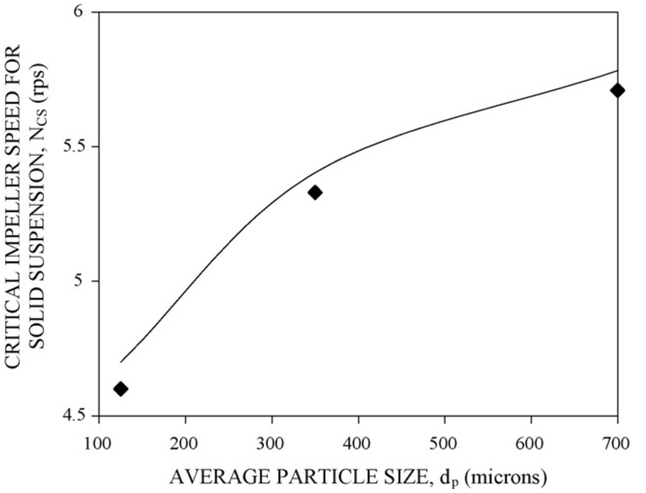

Fig. 10. Effect of average particle size on the critical impeller speed for PBTD45 ($X = 5$ wt.%, $\rho_p = 2400$ kg/m^3): (◆) experimental, (—) CFD predictions.

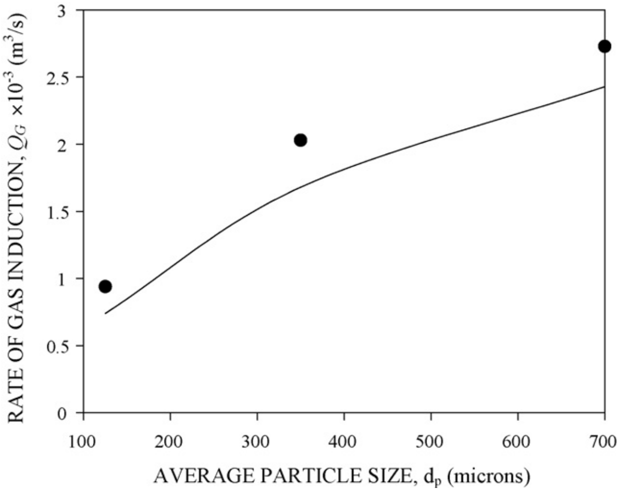

Fig. 12. Effect of average particle size on the gas induction rate for MDD ($X = 5$ wt.%, $\rho_p = 2400$ kg/m^3): (◆) experimental, (—) CFD Predictions.

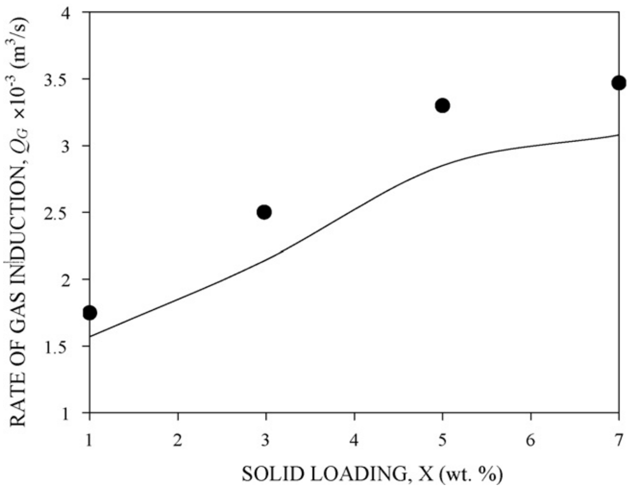

Fig. 13. Effect of solid loading on the gas induction rate for MDD ($d_p = 700\ \mu m$, $\rho_p = 2400\ kg/m^3$): (♦) experimental, (▬ CFD predictions.

5.4.3. *Effect of solid loading*

Similarly, EFD and CFD have been carried at N_{CS} for particles of average diameter 700 μm with solid loadings of 1, 3, 5 and 7 wt.%, respectively, for MDD. Fig. 13 shows the increase in the gas induction rate with an increase in the solid loading. This is mainly due to the corresponding increase in N_{CS}. It can be seen that the present CFD model slightly under predicts the gas induction rate in all the cases due to the complex and three-phase fluid dynamics prevailing in the system. The discrepancy between the prediction and the experimental results was probably because the model of inter-phase momentum exchange employed in the present work is too simple to describe the real complex inter-phase interaction coupling in gas–liquid–solid three-phase flows. Additionally, the isotropic k-ε two equation turbulence model is not sufficient in describing the well-recognized anisotropic nature of turbulent flow in stirred tanks. However, the prediction of the gas induction rates for different operating conditions can be improved by accounting all possible interactions among gas, liquid and solid phases along with some suitable modifications of model constant in the std k-ε turbulence model.

6. Conclusions

(1) Experiments have been performed for the measurements of the critical impeller speed for solid suspension and corresponding gas induction rate for the modified double disc, PBTD60, PBTD45 and PBTD30 self-inducing impellers.
(2) In the present work, three-phase stirred suspension has been simulated using FLUENT 6.2 CFD software. The Eulerian multi-fluid model along with the standard k-ε turbulence model has been used to simulate gas–liquid–solid dispersions.
(3) By using the concept proposed by Oshinowo and Bakker [19] has been extended for the prediction of critical impeller speed for solid suspension. The suggested value of σ holds for different impeller designs and over a wide range of particle size, solid loading.
(4) For three-phase hollow self-inducing system, the predicted critical impeller speeds have been compared with the in house experimental data for solid loading (0–7 wt. %), for different impeller designs (modified double disc (MDD) impeller, pitched blade down flow impellers of various angles (self-inducing PBTD60, PBTD45 and PBTD30 impellers), solid particle sizes (125–700 μm). A very good agreement was observed in all these cases.
(5) Further, the present CFD model was able to predict the gas induction rates based on the first principle. However, the discrepancies in the predictions of Q_G can be improved by employing more reliable inter-phase momentum exchange term and with some modification in the model parameters of std $k-\varepsilon$ model.
(6) Overall, the predicted gross characteristics of the fluid dynamics were presented and the computational model and the predicted results discussed in this work would be useful for providing better understanding of the flow characteristics and subsequent optimization studies.

Acknowledgement

Mr. B.N. Murthy and R.B. Kasundra acknowledge the Department of Atomic Energy and University Grant Commission (UGC), Government of India, respectively, for supporting this work.

References

[1] A.W. Patwardhan, J.B. Joshi, Design of gas inducing impellers, Ind. Eng. Chem. Res. 37 (1999) 49–80.
[2] J.B. Joshi, M.M. Sharma, Mass transfer and hydrodynamic characteristics of gas inducing type of agitated contactors, Can. J. Chem. Eng. 65 (1977) 683–695.
[3] N.A. Deshmukh, S.S. Patil, J.B. Joshi, Gas induction characteristics of hollow self-inducing impeller, Chem. Eng. Res. Des. 84 (2005) 124–132.
[4] B.N. Murthy, N.A. Deshmukh, A.W. Patwardhan, J.B. Joshi, Hollow self-inducing impellers: flow visualization and CFD simulation, Chem. Eng. Sci. 62 (2007) 3839–3848.
[5] G.R. Kasat, A.B. Pandit, Review on mixing characteristics in solid–liquid and solid–liquid–gas reactor vessels, Can. J. Chem. Eng. 83 (2005) 618–642.
[6] C.W. Wong, J.P. Wang, S.T. Haung, Investigations of fluid dynamics in mechanically stirred aerated slurry reactors, Can. J. Chem. Eng. 65 (1987) 412–419.
[7] T.N. Zwietering, Suspending of solid particles in liquid by agitators, Chem. Eng. Sci. 8 (1958) 244–253.
[8] P.L. Viollet, O. Simonin, Modelling dispersed two-phase flows: closure, validation and software development, App. Mech. Rev. 47 (1994) S80–S84.
[9] M. Ljungqvist, A. Rasmuson, Numerical simulation of the two phase flow in an axially stirred reactor, Chem. Eng. Res. Des. 79 (2001) 533–542.
[10] G. Montante, G. Micale, F. Magelli, A. Brucato, Experiments and CFD predictions of solid particle distribution in a vessel agitated with four pitched blade turbines, Chem. Eng. Res. Des. 71 (2001) 1005–1010.
[11] A.R. Khopkar, A.R. Rammohan, V.V. Ranade, M.P. Dudukovic, Gas–liquid flow generated by a Rushton turbine in stirred vessel: CARPT/CT measurement and CFD simulations, Chem. Eng. Sci. 60 (2005) 2215–2229.
[12] D. Pinelli, M. Nocentini, F. Magelli, Solids distribution in stirred slurry reactors: influence of some mixer configurations and limits to the applicability of a simple model for predictions, Chem. Eng. Comm. 188 (2001) 91–107.

[13] M.R. Bhole, J.B. Joshi, D. Ramakrishna, Population balance modeling for bubble column operating in the homogenous regime, AIChE J. 53 (2007) 750–756.

[14] FLUENT 6.2., User's Manual to FLUENT 6.2, Fluent Inc., Centrera Resource Park, 10 Cavendish Court, Lebanon, USA, 2005.

[15] J. Aubin, N.L. Sauze, J. Bertrand, D.F. Fletcher, C. Xuereb, PIV measurements of flow in an aerated tank stirred by a down-and an up-pumping axial flow impeller, Exp. Ther. Fluid Sci. 28 (2004) 447–456.

[16] A. Barresi, G. Baldi, Solid dispersion in an agitated vessel, Chem. Eng. Sci. 42 (1987) 2949–2956.

[17] R. Angst, M. Kraume, J. Ritter, Particle distribution and velocity in stirred vessels: experimental results and CFD-simulations, in: Proceedings of the Third International Symposium on Two-Phase Flow Modelling and Experimentation, Pisa, 2004, pp. 221–229.

[18] M. Bohnet, G. Niesmak, Distribution of solids in stirred suspension, Germ. Chem. Eng. 3 (1980) 57–65.

[19] I.M. Oshinowo, A. Bakker, CFD modelling of solid suspensions in stirred tanks, in: Symposium on Computational Modelling of Metals, Minerals and Materials, TMS Annual Meeting, Seattle, WA, 2002, pp. 234–242.

[20] A.R. Khopkar, G.R. Kasat, A.B. Pandit, V.V. Ranade, Computational fluid dynamics simulation of the solid suspension in a stirred slurry reactor, Ind. Eng. Chem. Res. 61 (2006) 2921–2929.